Article

Aerial Identification of Fruit Maturity in Amazonian Palms via Plant-Canopy Modeling

Willintong Marin [1], Ivan F. Mondragon [1] and Julian D. Colorado [1,2,*]

[1] School of Engineering, Pontificia Universidad Javeriana Bogota, Cra. 7 No. 40-62, Bogota, Colombia
[2] The OMICAS Institute, Pontificia Universidad Javeriana, Cali, 760031, Colombia
* Corresponding author: coloradoj@javeriana.edu.co

Abstract: UAV-captured multispectral imagery was used to characterize and associate Moriche's palm canopy features with the maturity stage of the corresponding fruits. Deep learning models based on convolutional neural networks (CNN) were trained in order to determine correlations between the photosynthetic radiation of the palms with the fruit. Here, we compare several approaches for feature extraction based on vegetation indices and graph-based models. Also, a comprehensive dataset has been collected and labeled, containing plant data for an entire phenological cycle of the Moriche palms. Experimental results reported an average estimation accuracy of 72%, by using the proposed method in dense forests of the Amazonian region.

Keywords: UAV; Deep Learning; Vegetation indices; graphs models; Mauritia Flexuosa Palm; Dense forests

1. Introduction

The Moriche palm (Mauritia Flexuosa) is a specie of the tropical moist forest, rich in proteins, fats, vitamins and carbohydrates [1–3]. The oil extracted from the Moriche fruits plays a significant role in the local economy [4–6]. Furthermore, the palm is also fundamental for the conservation of the Amazonian ecosystem, by regulating the neotropics wetlands of the forest [7]. Since this variety is mainly found in flooded areas within dense forests, remote sensing approaches are necessary to improve on crop monitoring and management practices [8].

In Colombia, The Amazonian Scientific Research Institute –SINCHI [1] recently published comprehensive data with the typology studies of Moriche's plant physiology and fruit maturity, concluding about the need of characterizing the stages of fruit maturity according to the phenological cycle of the palm, in order to determine biological correlations between the palm's canopy with the palm fruits. Based on that, remote sensing approaches could be introduced to speedup crop assessment practices, since the access to these dense forests is risky and time-consuming for the local communities [9]. To this purpose, we propose the integration and deployment of an unmanned aerial vehicle (UAV) equipped with multi-spectral sensors onboard, in order to automate the characterization process of fruit maturity by training deep-learning models. Figure 1 shows the Moriche palms located in dense forests of the Amazonian region of Colombia.

The use of UAVs with computer vision techniques for precision agriculture is well studied [10]. Several applications can be found for the estimation of chlorophyll, nitrogen, biomass, fruit counting, and maturity prediction in classical crops [11]. However, for unstructured crops located in dense forests, few works have been identified for Amazonian palms [12]. Based on the advances in the state of the art and the need to reduce the time and risks for fruit harvesting, in this work we propose the hypothesis to determine the state of maturity of the fruit through correlations with the canopy of the palm.

[1] https://www.sinchi.org.co/

 doi:10.20944/preprints202304.0496.v1

Figure 1. Moriche palms. In these dense forests of the Amazonian region, local communities access into these unstructured crops to both assess and gather the palm fruits manually.

1.1. Moriche's physiology

In plants, chlorophyll adsorbs the blue and red light radiation. Also, other bands of light are not adsorbed but reflected. In [13], Chlorophyll and carotenoids were identified as responsible for absorbing and converting light energy into chromophore molecules that respond to solar radiation, associating the green bands to Chlorophyll production and the yellow-orange bands with carotenoids. This molecular process is in charge of producing ethylene, which is a hormone that affects the leaf development, ripening, and flowering of many plants [13]. Through ethylene, is possible to determine correlations between ethylene fluctuations and fruit maturity.

Furthermore, in terms of plant morphology, the Moriche palms adjust the positions of their leaves over their neighbors at the same altitude of the plant canopy, to avoid a reduction in light incidence, especially the red/far red ratio. The leaves contain an organ, the Pulvinus, that controls their movement according to light-darkness. During the day, the leaflets are open and in a horizontal position, while at night, they are closed in a vertical position. The Pulvinus is approximately 2-7mm in length and 2-3mm in diameter. The flowering process of a species occurs synchronously for all individuals in the same geographical area to ensure their genetic exchange and reproductive success. During the fruiting process, there is a relationship between the leaf and fruit, and the elimination of leaves at the beginning of the cell division phase of the fruit leads to a decrease in sucrose. In this regard, ethylene is not only activated in large quantities during the fruit ripening process, but is also activated during leaf abscission and floral senescence [13].

As observed in Figure 1, the Moriche palm is a tall tree that can grow up to 40 meters in height. It has a spherical crown and palmate leaves, usually between 11 to 14 in number, which can be 2.5 to 4.5m long and wide, respectively. The leaves are divided into about 200 segments. The palm produces up to 8 inflorescences, which emerge from between the leaves. The fruit is elliptical, 7cm long and 5cm in diameter, and when ripe, it is dark orange-red to reddish-brown, fleshy, and oily. The Moriche palm grows in temporarily or permanently flooded lands and forms large populations called cananguchales, aguajales or morichales. The fruit growth and development of the Moriche palm lasts for around 250 days, and generally has a single seed. Fruits exhibit typical climacteric behavior during the initial stage of development, while finally entering a period of stability until maturity. There is an absence of ethylene levels during the sampling periods. [8]

Also, the right plots of Figure 1 details the inflorescence of the palms. Flowering takes between two and eight months, and fruiting between 10 and 12 months. However, the beginning of these processes varies in each region; in the Guaviare Amazon area of

 doi:10.20944/preprints202304.0496.v1

Maturity State	Typology	Color description
	Green	100% bright green fruit
	Pinton 1	Bright green fruits with 3/4 bright orange
	Pinton 2	Bright orange fruits with 2/4 dull green
	Pinton 3	Bright orange fruits with 3/4 dull green
	Ripe	Opaque brown fruits 100% of the fruit surface

Figure 2. Moriche fruit maturity typology.

Colombia, female flowering occurs between May and July during the period of heavy rains, and between August and December, a period in which rainfall decreases slightly. The inflorescence occur between the leaves, each with up to 100,000 male flowers and 6,000 female flowers [14]. One palm produces between 4 and 8 bunches per year, each with up to 730 fruits, weighing 85 grams. From one palm, 100 to 200 kg of fruit can be extracted. Each fruit takes approximately 4 months to grow and 4 more months to ripen [14]. Figure 2 shows the 5 types of maturity stages, by following the classification presented by [5].

1.2. Feature extraction

Vegetation indices (VIs) have become an essential model to extract plant's features, by combining different wavelengths associated with the plant light reflectances. In this work, we conducted a comprehensive literature review in order to identify vegetation indices associated with canopy structure, atmospheric stress, Chlorophyll production, biomass and leaf nitrogen dynamics, plant senescence and palm inflorescence.

The authors in [15] proposed a method of land classification using vegetation indices based on the visible spectrum - VDVI (visible band difference vegetation index). In general RGB-based vegetation indices are sensitive to plant greenness [16]. In [17], it was found that the Green-Red Vegetation Index (GRVI) was an efficient phenological indicator for calculating biomass. Also, the Modified green red vegetation index (MGRVI) allowed to amplify the reflectance differences between the bands, thus increasing the estimation of plant biomass as a function of predicting chlorophyll content [18].

In [19], other vegetation indices are introduced, such as the Visible Atmospheric Resistance Index (VARI) and the Normalized Green-Red Difference Index (NGRDI), which are used to estimate the vegetation fraction. Others such as the excess green index (ExG) and the color index of vegetation (CIVE) have also been tested to identify green vegetation. Also, [20] found a strong correlation for the Normalized Difference Vegetation Index (NDVI) with the estimation changes in the maturation stage of plants [21]. Other authors combined several vegetation indices to increase estimation correlations. For instance, [20] were able to identify variations in chlorophyll between crop growth, flowering and fruiting. They identified that chlorophyll at canopy level is lower at fruiting.

Preprints (www.preprints.org) | NOT PEER-REVIEWED | Posted: 18 April 2023 doi:10.20944/preprints202304.0496.v1

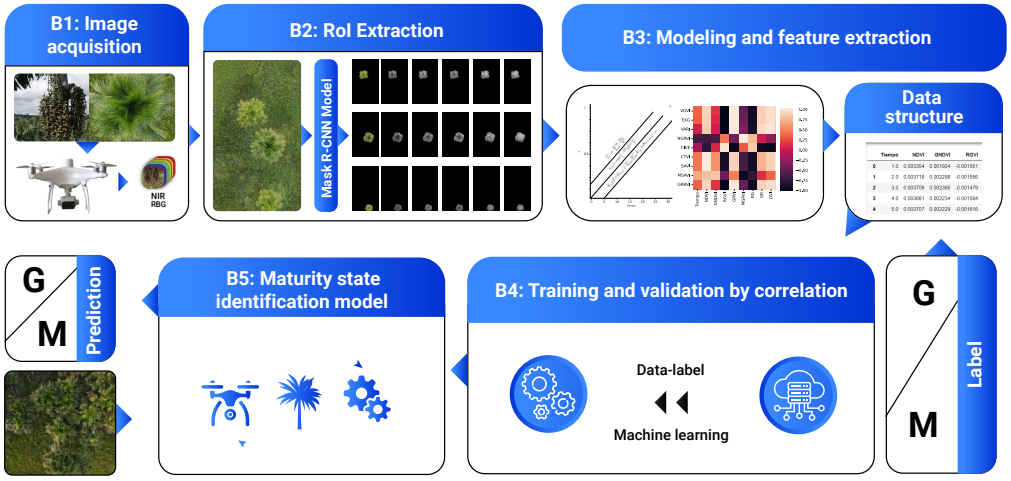

Figure 3. System architecture.

Although vegetation indices have been widely used to study different plant phenomena based on plant light reflectances, to the best of the author's knowledge, there is not published research regarding the study of the physiological conditions of canopy-fruits for the these Amazon species. Furthermore, in this work, we also propose to evaluate other features besides vegetation indices, based on the recent results presented in [22], by applying graph-based data fusion methods using the multi-spectral data imagery.

2. Materials and Methods

Figure 3 presents the proposed system architecture. There are five modules that make up the multispectral image acquisition process for palm fruit identification. Module B1 is responsible for acquiring the multispectral images, which are composed of 5 bands (R, G, B, RE and NIR) as well as the RGB image. In module B2, a palm identification model is used to segment and extract the Region of Interest (RoI) from each band. Module B3 conducts a temporal variability analysis and modeling of each feature to identify their response and correlation with the maturity stages of the fruit. The resulting data is then structured and properly labeled. Module B4 trains, validates and tests the Machine Learning (ML) models for identifying fruit maturity stages through correlations. Finally, module B5 performs the segmentation steps with the ML model, feature extraction on the RoI and estimates the fruit maturity by correlating with the photosynthetic radiation of the canopy.

2.1. Protocol for image acquisition

UAV flight missions were organized on a biweekly basis for one year, from October 2020 to September 2021, in order to capture multispectral imagery of palm plots located in the Department of Guaviare, Colombia, as depicted in 4. Imagery was captured at altitudes of 60, 90, and 120 meters above ground level using the multispectral camera mounted on a Phantom 4 Multispectral UAV, with a resolution of 2.08MP per band. The image size was 1600×1300, with a resolution of 3.2cm/pixel at 60 meters altitude. UAV waypoints were used to cover each palm within the delimited plots. the UAV autopilot was used to ensure that the camera captured images at the canopy level to cover the crown, and manual pilot mode was used to monitor the fruiting or inflorescence state of each individual palm by bringing the drone as close as possible to the surrounding vegetation. Relevant weather information such as temperature, wind speed, and sky conditions were captured for each flight.

The following criteria were established for the flight mission: images were classified, labeled, and stored by date, genus, while labeling based on the state of the plant and fruit. The aforementioned procedure is detailed as follows:

Preprints (www.preprints.org) | NOT PEER-REVIEWED | Posted: 18 April 2023 doi:10.20944/preprints202304.0496.v1

Figure 4. Geolocation of dense forest crops in the Colombian Amazon. Waypoints detail the UAV trajectory.

- General Conditions: first, palms were selected by their genus and species and georeference the location of each palm. Then, palms were physically marked with reflective tape to differentiate between genders. Next, imagery was captured around each palm at a distance of less than 3 meters, with a manual pilot following a polygon way-point path. A dataset was created in the acquired images, along with the palm, fruit and weather conditions. To ensure consistency in the physiological state between the fruits and the canopy, days with similar illumination and solar radiation were selected for the UAV mission. A weekly flight was conducted for each variety, with local time between 9-11am and 3-5pm.
- Canopy level: The UAV conducted mission flights at a general altitude of 60, 90, and 120 meters. Lower altitudes could result in partial or total exclusion of the palm due to geolocation precision and climatic factors.
- Fruit level: to capture images of the clusters in each palm, a manual flights were conducted, ensuring that there is enough space around each palm to maneuver the UAV and avoid collisions. Images should be captured of each cluster from multiple angles, distances, and heights, with a focus on capturing images as close as possible. Additionally, images of the fruits and inflorescence were captured. The canopy around the palm and at the top should also be captured at various heights and distances.
- Segmentation (RoI): The Region of Interest (RoI) was extracted by applying a Mask R-CNN-based algorithm for object identification developed by the authors in previous work reported in [23]. Since the object detector of the original algorithms works with RGB images, a sub-process was designed for the extraction of the RoI to all spectral bands.

2.2. Feature Extraction

Vegetation indices

We selected 25 vegetation index features as detailed in 1. Each feature C_i is composed of the mean of the vector obtained by calculating the vegetation index in each region of interest, as described by Eq. (1). Also, Eq. (2) allows us to model the behavior of each index, by considering all the features extracted per flight C_T.

$$C_i = \sum_i^n \frac{IV_i}{n} \tag{1}$$

$$C_T = \sum_i^n \frac{CT_i}{n} \tag{2}$$

Graphs

Networks are composed of nodes and edges that contain highly relevant information and data, which we can process and extract for estimation purposes. Nodes belonging to a graph can interrelate with nodes of other graphs and bring out information not perceptible by other methods, such as the vegetation indices. In this way, we can calculate the relationships of the data of each channel contained in an image.

Preprints (www.preprints.org) | NOT PEER-REVIEWED | Posted: 18 April 2023 doi:10.20944/preprints202304.0496.v1

Table 1. VIS-NIR Vegetation Indices listed

VI	Descripción	Expresión matemática
GRVI	black Vegetation Index [24]	$\frac{G-R}{G+R}$
RGVI	Green Vegetation Index [18]	$\frac{R-G}{R+G}$
MGRVI	Modified black Vegetation Index [24]	$\frac{G^2-R^2}{G^2-R^2}$
NGRVI	Reciprocal transformation based on MGRVI normalization [17]	$\frac{1}{MGRVI}$
GRBVI	Normalized green-black difference index [25]	$\frac{G^2-RB}{G^2+RB}$
VARI	Visible Atmospherically Resistant Index [24]	$\frac{G-R}{G+R-B}$
RG	black Green Ratio [26]	$\frac{R}{G}$
GR	black Green Ratio Index [16]	$\frac{G}{R}$
VDVI	Visible-band difference vegetation index [25]	$\frac{2G-R-B}{2G+R+B}$
EXG	Excess green [25]	$2G-R-B$
CIVE	Color Index of Vegetation [19]	$0.441R-0.881G+0.385B+18.787$
NGBDI	Normalized green-blue difference index [27]	$\frac{G-B}{G+B}$
NRBDI	Normalized black-blue difference index [18]	$\frac{R-B}{R+B}$
RGBVI	black, Green-Blue Vegetation Index [18]	$\frac{R-G}{R+G+B}$
RBGVI	black, Blue-Green Vegetation Index [18]	$\frac{R-B}{R+G+B}$
NIRG	Green model [28]	$\frac{NIR}{G}-1$
NIRRE	Red border model [28]	$\frac{NIR}{RE}-1$
NDVI	Normalized difference vegetation index [20]	$\frac{NIR-R}{NIR+R}$
RVI	Ratio Vegetation Index [29]	$\frac{NIR}{R}$
DVI	Difference Vegetation Index [30]	$NIR-R$
GNDVI	Green NDVI [31]	$\frac{NIR-G}{NIR+G}$
CTVI	Corrected Transformed Vegetation Index [30]	$\frac{NDVI+0,5}{\lvert NDVI+0,5\rvert}\sqrt{NDVI+0,5}$
SAVI	Soil-Adjusted Vegetation Index [31]	$\frac{NIR-R}{NIR+R+L}, conL=0,5$
MSAVI	Modified SAVI [32]	$\frac{1}{2}(2NIR)+1-\sqrt{(2NIR+1)^2-8(NIR-R)}$
NBVI	Green NDVI	$\frac{NIR-B}{NIR+B}$

Graph-based methods usually use the Nyström extension theory [33–36] in order to determine relevant features from a set of data, while applying a comprehensive dimensionality reduction to finally select the most accurate features. To generate the graph, we use the model described in Eq. (4), which allows to identify temporal changes in photosynthetic radiation of the palms. Each band of the images contains pixels that can be interpreted as a sign of a graph, which are connected pixel-by-pixel in each band with its neighbor. The graph is defined as $G=(V,E)$ where G is the graph, V is the set of nodes and E is the set of edges that describes the direct relationship between nodes. An edge connects two nodes, while a node can be connected by more than 2 nodes through the edges. The feature vector is obtained from the spectrum of the eigenvectors, while the mean of the vector is considered for the corresponding modeling. The relationships among nodes are quantified by a weight given by $w_{i,j}$, as also described by Eq. (3).

$$w_{i,j}=exp\left(-\frac{d(V_i,V_j)^2}{\sigma^2}\right) \tag{3}$$

Where $d(V_i,V_j)$ corresponds to the Euclidean distance between associated pixel values and σ is the standard deviation of all the $d(V_i,V_j)$.

$$C_v=\sum_i^n \frac{V_p}{n} \tag{4}$$

Where C_v is the mean of the full vector of eigenvalues for each RoI. In this way, we can observe the temporal behavior of the variable throughout the phenological cycle and compare the performance with the vegetation indices.

Convolutional Neural Networks (CNN)

CNNs have become the fundamental basis for large-scale object detection using deep-learning [37]. Figure 5 presents the CNN-based model used in this work, consisting of 2 main modules: i) a feature extractor, which are basically composed of a series of convolutional filters applied to the input image to generate a feature map, ii) a fully connected layer classifier. The convolution process is the summation of the pixel by pixel scalar product between the input matrix and the defined kernel. The size of the feature map

Preprints (www.preprints.org) | NOT PEER-REVIEWED | Posted: 18 April 2023 doi:10.20944/preprints202304.0496.v1

depends on the size of the kernel and the defined strides, usually 2×2, 3×3 kernels and 1, 2 or 3 strides. Equation ((5)) describes the convolution filters, whereas Eq. ((6)) represents the non-linearity Activation Function ReLU/Rectified Linear Unit. Equation ((7)) describes the max-pooling or maximum pixel clustering for each defined window, which reduces the feature map.

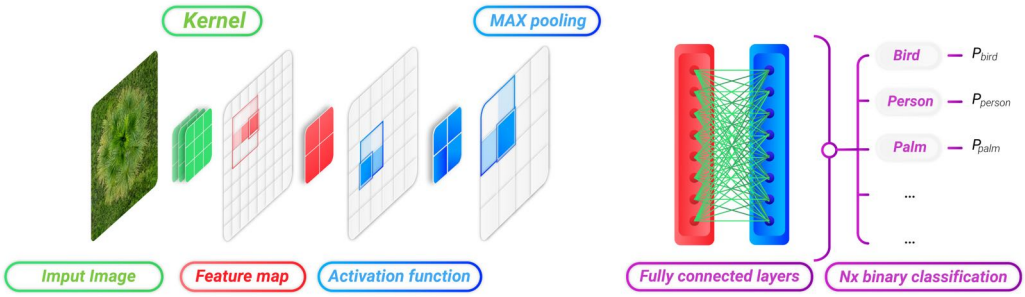

Figure 5. Convolutional neural network.

$$S_{i,j}(I * k)_{i,j} = \sum_m \sum_n I_{i,j} * K_{i-m,j-n} \tag{5}$$

$$ReLU(x) = \begin{Bmatrix} x, & x \geq 0 \\ 0, & x < 0 \end{Bmatrix} \tag{6}$$

$$Max(0, x) = \begin{Bmatrix} x, & x \geq 0 \\ 0, & x < 0 \end{Bmatrix} \tag{7}$$

2.3. Data modeling and classification

The data modeling process involves studying the relationship between the variables of VI and graphs with the time variable. Pearson's correlation coefficient is used to determine the strength of the relationship between two variables. When there is a positive relationship, the model has a positive slope, and when there is an inverse relationship, the model has a negative slope. A covariance of approximately zero indicates no relationship. Equation 8 provides the mathematical expression for Pearson's correlation coefficient, where r is the coefficient and takes values between -1 and 1. A value of r close to 1 indicates a strong positive correlation, while a value close to -1 indicates a strong inverse correlation. Coefficients close to zero indicate no linear correlation. The symbol σ_{xy} represents covariance, while σ_x and σ_y represent the standard deviation of x and y, respectively.

$$r = \frac{\sigma_{xy}}{\sigma_x * \sigma_y} \tag{8}$$

In the process of estimating the state of maturity through correlations, the vegetation indices (VI) and graph data are structured for training machine-learning (ML) models. Three datasets were assembled and used for training and testing: datasets CD1 with 25 VI, datasets CD2 with 50 network characteristics, and datasets CD3 with 25 VI and the sum of the components per network, resulting in a total of 26 characteristics. The datasets were separated into two states of maturity, C1 (class 1) for green, pinton 1, and pinton 2, and C2 (class 2) for pinton 3 and mature, as previously described in Figure 2.

For training and validation, we used Lazy Predict[2], a tool that compiles a set of classification and regression models, delivering result metrics such as accuracy, ROC-AUC, F1-Score, and processing time. Additionally, a conventional Artificial Neural Network was trained with 2 hidden layers with a Rectified Linear Unit (ReLU) as activation functions, and an output layer with a Sigmoid activation function, binary cross-entropy loss function and Adam optimizer, with a learning rate of 0.001, and 100 epochs.

[2] https://lazypredict.readthedocs.io/en/latest/index.html

Preprints (www.preprints.org) | NOT PEER-REVIEWED | Posted: 18 April 2023 doi:10.20944/preprints202304.0496.v1

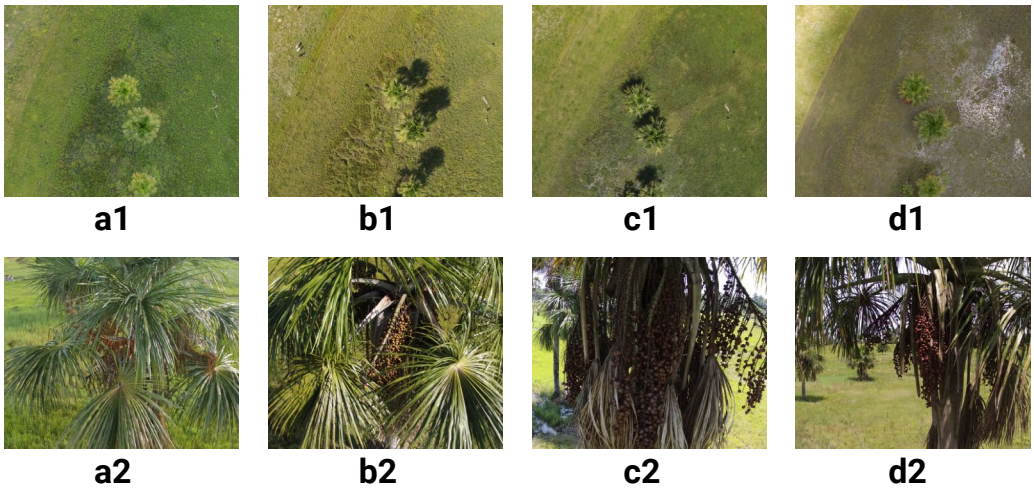

Figure 6. Moriche palm phenological cycle. Insets a1-d1 corresponds to the months of October, January, April and July. Insets a2-d2 detail the inflorescence and the palm fruits maturity.

Finally, a CNN was trained with a 200 × 200 RGB images using data augmentation techniques. It consisted of one layer of 32 3 × 3 filters with a Relu activation function, one layer of 64 3 × 3 filters with a ReLU activation function, and one layer of 128 3 × 3 filters with a ReLU activation function. The 2 × 2 Maxpooling function was applied after each layer. The Bynary Crossentropy loss function and the Adam optimizer were configured for 100 epochs, step size of 32, two classes (Green and Mature) and a learning rate of 0.0005.

3. Results

An entire phenological cycle was captured from October 2020 to September 2021, where 60 UAV flight missions were conducted. Table 2 details the corresponding data.

Table 2. Moriche palms datasets. Two crop plots were evaluated to ensure the proper spatial repetition.

Plot	# flights	# UAV waypoints	# images
Plot 1	30	18	540
Plot 2	30	51	1530

Figure 6 depicts several aerial views of the Moriche species in plot 1. The multispectral imagery contains 5 bands separately: Red, Green, Blue, Red Border and NIR.

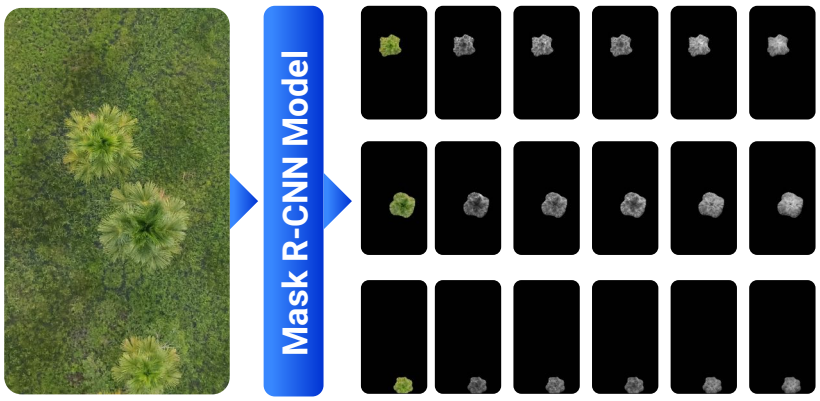

Figure 7. Extraction of RoI from each spectral layer. From left to right the RoI in RGB, followed by the R, G, B, ER and Nir bands separately.

Preprints (www.preprints.org) | NOT PEER-REVIEWED | Posted: 18 April 2023 doi:10.20944/preprints202304.0496.v1

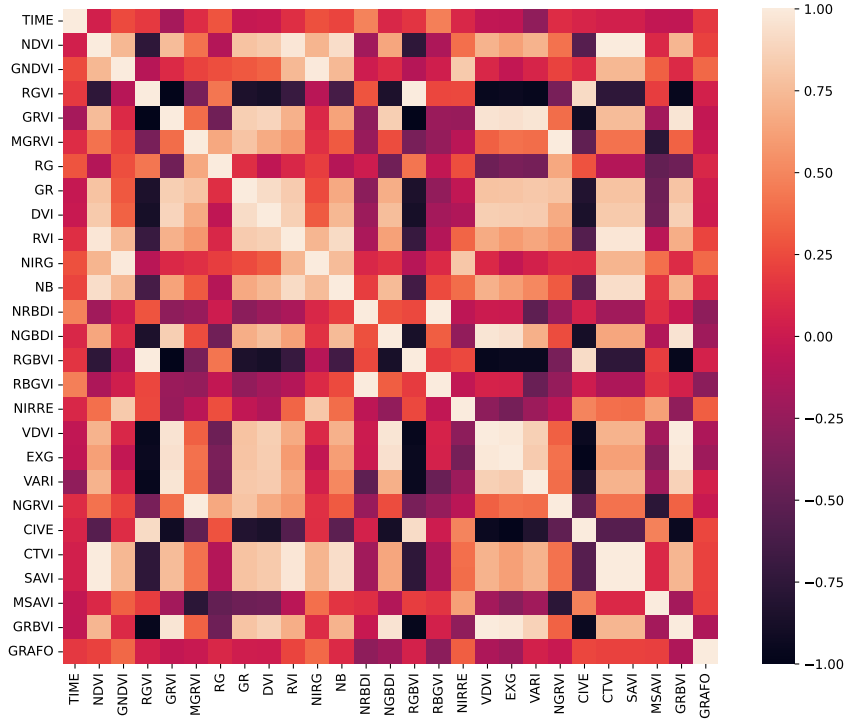

Figure 8. Pearson correlation map relating the 25 VI and Graph characteristics (named GRAFO) as an average vector. The bar on the right side indicates the strength of the correlations.

Using the Moriche palm identification and segmentation model, the images obtained from plot 1 are processed to extract Region of Interest (RoI) characteristics. The path of this plot contains 18 points or images, resulting in 59 palms and 59 RoI for each of the 30 flights during the phenological year. The algorithm extracts the RoI from all 5 spectral layers of the image. Therefore, from the 18 images captured per flight, 59 RoI per layer are generated, resulting in a total of 295 RoI across all layers in each flight. Figure 7 shows the regions of interest for all bands, extracted from an image containing 3 palms.

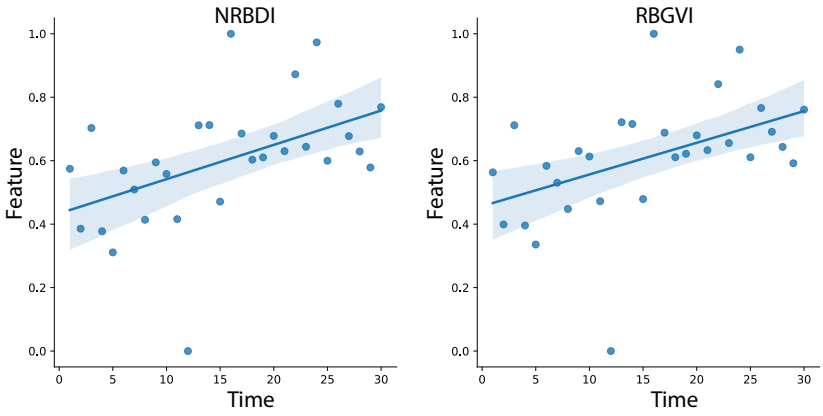

Figure 9. Linear correlation of NRBDI, RBGVI characteristics with moderate correlation.

Applying the aforementioned 25 Vegetation Indices (VI) for feature extraction in each image RoI, a dataset of 1770 instances is constructed. Similarly, a dataset of 50 features per 1770 instances is constructed with the graphs. To determine the temporal changes of the

Preprints (www.preprints.org) | NOT PEER-REVIEWED | Posted: 18 April 2023 doi:10.20944/preprints202304.0496.v1

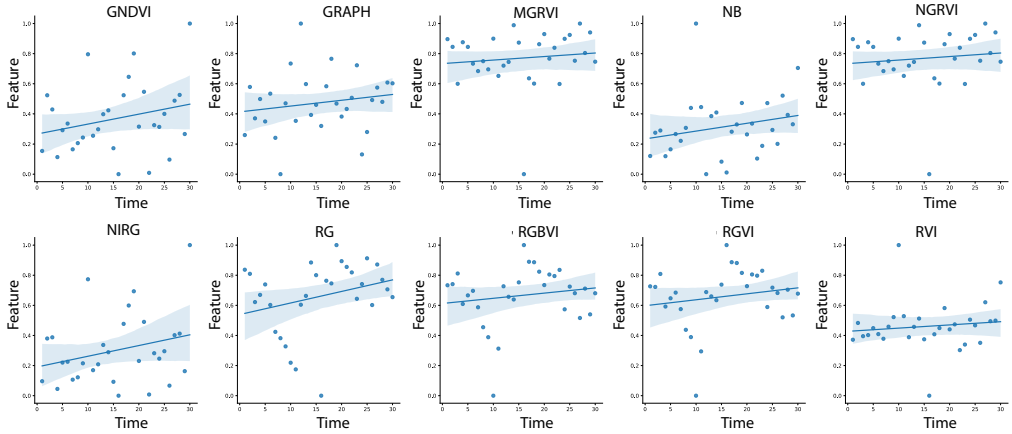

Figure 10. Linear correlation of features GNDVI, RGVI, MGRVI, RG, RVI, NIRG, NB, RGBVI, NGRVI, and Graph with low correlation.

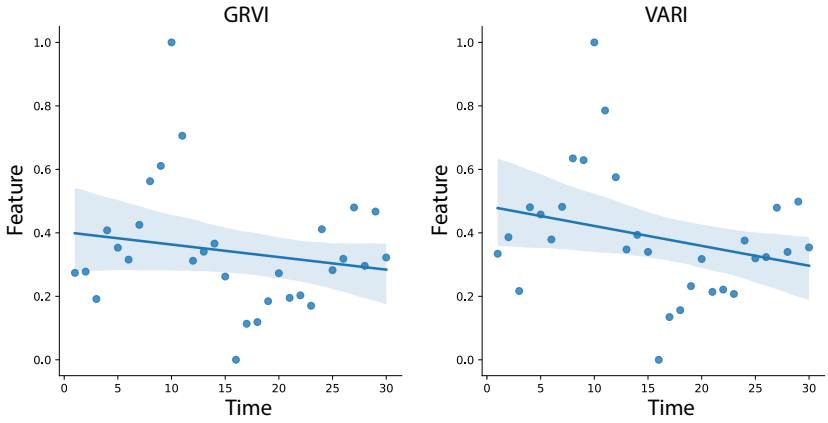

Figure 11. Linear correlation of GRVI and VARI features with low negative correlation.

data during the phenological cycle, pearson's model is applied to all the data. Figure 8 shows the pearson map with the strength of relationships between each variable (VI and graphs) with the time variable ranging from 1 to 30.

The Pearson correlation map, also known as the heat map of the correlation matrix, ranges from 1 to -1, and shows the color relationships ranging from light to dark. Light colors correspond to 1 and dark corresponds to -1. The map shows a moderate relationship for NRBDI and RBGVI indices, low correlation for GNDVI, RGVI, MGRVI, RG, RVI, NIRG, NB, RGBVI, NGRVI, Grafo, and low negative correlation for GRVI and VARI. The other characteristics such as NDVI present a low linear correlation. Figures 9, 10, and 11 detail the linear behavior of the characteristics with moderate, low, and negative correlation respectively. Table 3 summarizes the numerical results.

For the estimation of fruit maturity, the training and validation of Machine Learning (ML) models are performed. As mentioned, the dataset is divided into 2 classes (Green and Mature), with 1758 out of 1770 data are available. Twelve false positives were found in the RoI review, which were eliminated from the datasets. For the Convolutional Neural Network (CNN) training and validation process, the dataset for 2 classes (green and mature) was used. Figure 12 shows the results of this process for 100 epochs. The curve for training has an acceptable behavior as the epochs evolves, and the error decreases. However, in the accuracy curve, the error fluctuates, which means that the classification result is not predictable. To test the model, three new datasets with 100 instances each were used (50 for the green class and 50 for the mature class). Table 4 corresponds to the confusion matrices generated by training a CNN at 100 epochs with an accuracy of 53%, 54% and 48% respectively.

Preprints (www.preprints.org) | NOT PEER-REVIEWED | Posted: 18 April 2023 doi:10.20944/preprints202304.0496.v1

Table 3. Ratio of the correlation coefficients of the characteristics with moderate, low and low negative correlation.

Characteristic	Coefficient	Ratio
NRBDI	0.482360	Moderate
RBGVI	0.465781	Moderate
RG	0.284647	Low
NIRG	0.268070	Low
GNDVI	0.248591	Low
NB	0.224336	Low
RGVI	0.178566	Low
Grafo	0.170969	Low
RGBVI	0.155478	Low
RVI	0.117775	Low
MGRVI	0.110696	Low
NGRVI	0.110696	Low
GRVI	-0.178566	Low negative
VARI	-0.274951	Low negative

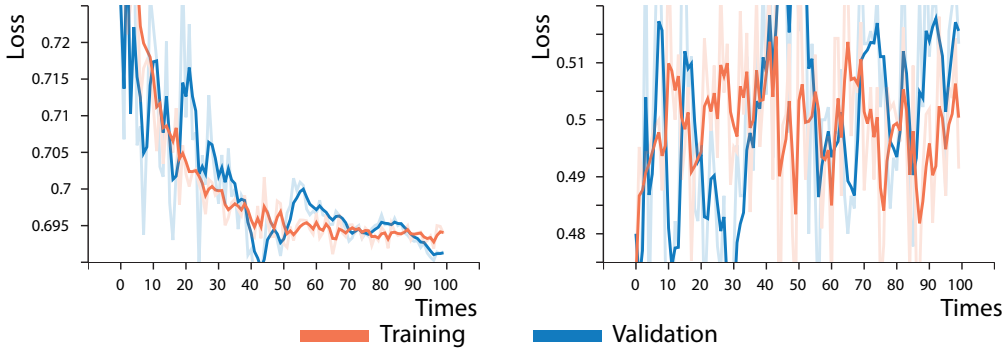

Figure 12. Loss and accuracy curve for training and validation of the CNN. The left plot corresponds to the loss curve, while the right plot corresponds to the accuracy curve.

Table 4. Dataset confusion matrix numerical results

Dataset 1			
Class	FP	TP	Total
CV	26	24	50
CM	21	29	50
Total	47	53	100
Accuracy	47%	53%	100%

Dataset 2			
Class	FP	TP	Total
CV	34	16	50
CM	12	38	50
Total	46	54	100
Accuracy	46%	54%	100%

Dataset 3			
Class	FP	TP	Total
CV	31	19	50
CM	21	29	50
Total	52	48	100
Accuracy	52%	48%	100%

Table 5 corresponds to the results obtained from training the ML models using the Scikit-learn Lazy-Predict tool. This tool helps us to identify the best models. The highest accuracy attained during the training process was 70%. The training of 7 ML models was performed using the same dataset. Figure 13 shows the ROC curve that corresponds to the training and validation outcomes. It should be noted that the Linear Regression (LR) model exhibits the best performance, with an accuracy of 70%. Also, Figure 14 shows the three ROC curves that correspond to the training an ANN using three different feature groups. The group that presents the poorest accuracy is the one that includes only graphs, with an accuracy of 52%. In contrast, the VI data combined with the graphs obtained the same result of 72%.

4. Discussion

The experimental results presented in this work are step closer in determining correlations of fruit maturity stage with plant canopy photosynthetic radiation data. Collaborative and interdisciplinary work with experts in plant physiology could significantly contribute to identifying the physicochemical variables of plants, deepening the correlations. Similarly, significant progress has been made in identifying the maturity stage through correlations,

Preprints (www.preprints.org) | NOT PEER-REVIEWED | Posted: 18 April 2023 doi:10.20944/preprints202304.0496.v1

Table 5. Classification results of ML Models integrated in the Lazy Predict tool. The first column refers to the ML model, the second to the accuracy achieved by each model, the third to the F1 Score and the fourth is the training and validation time.

Model	Accuracy and F1 Score	Time	
RidgeClassifier	0.7	0.7	0.02
LinearSVC	0.7	0.7	0.09
CalibratedClassifierCV	0.7	0.7	0.33
LogisticRegression	0.7	0.7	0.04
RidgeClassifierCV	0.69	0.69	0.02
LinearDiscriminantAnalysis	0.68	0.68	0.02
NuSVC	0.66	0.66	0.12
Perceptron	0.66	0.66	0.02
QuadraticDiscriminantAnalysis	0.66	0.66	0.02
SVC	0.66	0.66	0.07
AdaBoostClassifier	0.64	0.64	0.19
ExtraTreesClassifier	0.64	0.64	0.21
LGBMClassifier	0.64	0.64	0.11
RandomForestClassifier	0.64	0.64	0.34
XGBClassifier	0.63	0.63	0.11
SGDClassifier	0.63	0.63	0.02
PassiveAggressiveClassifier	0.61	0.58	0.01
KNeighborsClassifier	0.62	0.62	0.04
BaggingClassifier	0.61	0.61	0.12
LabelSpreading	0.60	0.60	0.10
LabelPropagation	0.60	0.60	0.08
ExtraTreeClassifier	0.54	0.54	0.01
DecisionTreeClassifier	0.54	0.54	0.03
GaussianNB	0.55	0.52	0.01
NearestCentroid	0.54	0.54	0.01
BernoulliNB	0.54	0.53	0.01
DummyClassifier	0.46	0.46	0.01

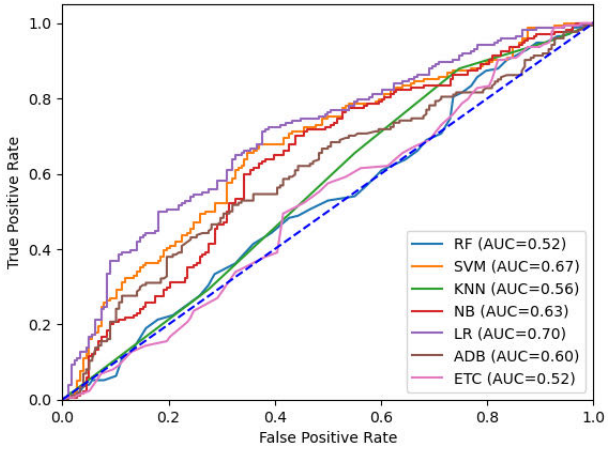

Figure 13. ROC curve for 7 ML models trained with 25 vegetation indices.

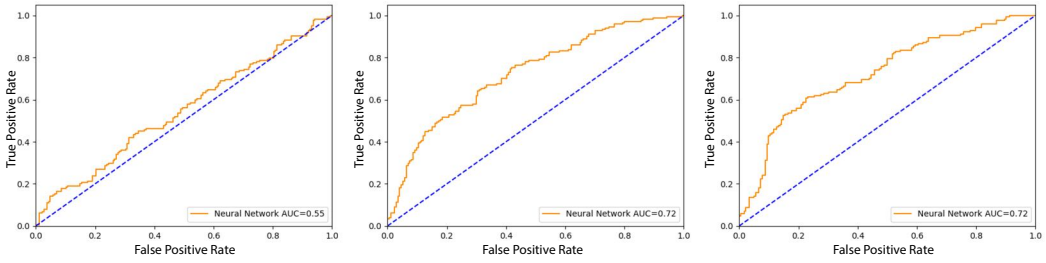

Figure 14. ROC curve obtained with the ANN model: (left) graph-based features, (middle) vegetation index features, (right) vegetation index and graph-based features combined.

but precision in classification must improve for industrial work. Only five spectral channels were used in this study, and the use of more channels could substantially improve results.

According to Azcon-Bieto (2003), ethylene affects leaf development and controls leaf expansion. Plants modify the positions of their leaves over their neighbors, horizontally and vertically in the canopy, to avoid reduction of light incidence, mainly the red/far red ratio. These movements could be detected through characteristic graphs or Convolutional Neural Networks (CNNs), but only if there were sufficient changes throughout the phenological cycle. However, according to classification results through correlations, these changes occur for very short periods and insufficient time rates to be detected.

5. Conclusions

We found a significant correlation between canopy photosynthetic radiation and fruit maturity stage. Out of the 25 vegetation indices, NRBDI and RBGVI showed a moderate correlation with the temporal variable. These indices used a combination of bands in the visible spectrum, specifically red and blue bands for NRBDI and red, blue, and green bands for RBGVI. However, several indices utilizing the near infrared band demonstrated low correlations, which is important for classification processes. In the same group with low correlation, we found extracted features through graphs, however, the VIs contributed the most as features. The performance of the network with these features was approximately 50%. The best performing classifiers were Artificial Neural Networks and Logistic Regression. The results of classifying with Convolutional Neural Networks were not accurate, achieving only 52% precision on average, over the three datasets. This result supports two theories: either CNNs perform best in object identification processes or we did not obtained enough changes in the canopy at the morphological level that corresponded to the fruit's maturity stage. Overall, the ANN models obtained an accuracy of 72%.

Author Contributions: Conceptualization, W.M., J.D.C. and I.F.M.; methodology, W.M., J.D.C. and I.F.M.; software, W.M.; validation, W.M.; formal analysis, W.M., J.D.C. and I.F.M.; investigation, W.M.; resources, , W.M.; data curation, W.M., J.D.C. and I.F.M.; writing—original draft preparation, W.M.; writing—review and editing, J.D.C. and I.F.M.; visualization, W.M., J.D.C. and I.F.M.; supervision, J.D.C.; project administration, W.M.; funding acquisition, W.M. All authors have read and agreed to the published version of the manuscript.", please turn to the CRediT taxonomy for the term explanation. Authorship must be limited to those who have contributed substantially to the work reported.

Funding: This work is funded by the Department of Guaviare and the Ministry of Science, Technology and Innovation (MinCiencias) of Colombia. Call No. 752 of 2016. *High-level human capital training for the Department of Guaviare, 2016 - II cohort, to finance doctoral studies*. Also by the OMICAS program: "Optimización Multiescala In-silico de Cultivos Agrícolas Sostenibles (Infraestructura y validación en Arroz y Caña de Azúcar)", anchored at the Pontificia Universidad Javeriana in Cali and funded within the Colombian Scientific Ecosystem by The World Bank, the Colombian Ministry of Science, Technology and Innovation, the Colombian Ministry of Education, the Colombian Ministry of Industry and Tourism, and ICETEX, under grant ID: FP44842-217-2018 and OMICAS Award ID: 792-61187.

Acknowledgments: The authors thank the SINCHI Amazon Institute for its support to the research. Likewise, the company Smart Life Technology SAS is thanked for the UAV equipment for capturing the images.

Conflicts of Interest: The authors declare no conflict of interest. The funders had no role in the design of the study; in the collection, analyses, or interpretation of data; in the writing of the manuscript; or in the decision to publish the results.

References

1. Maciel, E.A.; Martins, F.R. Rarity patterns and the conservation status of tree species in South American savannas. *Flora: Morphology, Distribution, Functional Ecology of Plants* **2021**, *285*, 151942. https://doi.org/10.1016/j.flora.2021.151942.

2. Navarro-Cruz, A.R.; Lazcano-Hernández, M.; Vera-López, O.; Kammar-García, A.; Segura-Badilla, O.; Aguilar-Alonso, P.; Pérez-Fernández, M.S. Mauritia flexuosa L. f. In *Fruits of the Brazilian Cerrado*; Springer, Cham, 2021; pp. 79–98. https://doi.org/10.1007/978-3-030-62949-6_5.
3. Velarde V., M.J.; Moraes R., M. Densidad de individuos adultos y producci ón de frutos del asaí (Euterpe precatoria, Arecaceae) en Riberalta, Bolivia. *Ecología en Bolivia* **2008**, *43*, 99–110.
4. Quintero-Angel, M.; Martínez-Girón, J.; Orjuela-Salazar, S. Agroindustrial valorization of the pulp and peel, seed, flour, and oil of moriche (Mauritia flexuosa) from the Bita River, Colombia: a potential source of essential fatty acids. *Biomass Conversion and Biorefinery* **2022**, *1*, 1–9. https://doi.org/10.1007/s13399-022-02298-3.
5. SINCHI. *Fichas Palmas amazónicas con potencial Seje, Moriche y Asaí*; 2018.
6. Ponce, M.E. Patrones de caída de frutos en Mauritia Flexuosa L.F. y fauna involucrada en los procesos de remoción de semillas. *Acta Botánica Venezuelica* **2002**, *25*, 119–142.
7. van der Hoek, Y.; Solas, S.Á.; Peñuela, M.C. The palm Mauritia flexuosa, a keystone plant resource on multiple fronts, 2019. https://doi.org/10.1007/s10531-018-01686-4.
8. Hernández, M.S., Castro, S.Y., Giraldo, B., Barrera, J. *Seje, moriche, asaí: Palmas amazónicas con potencial*, primera ed ed.; Diana Patricia Mora Rodríguez: Bogotá D.C., Colombia, 2018; p. 123.
9. Cárdenas López, D.; Arias G., J.C. *Manual de identificación, selección y evaluación de oferta de productos forestales no maderables*; 2007; p. 32 páginas.
10. Ponce-Corona, E.; Guadalupe Sánchez, M.; Fajardo-Delgado, D.; Acevedo-Juárez, B.; De-La-Torre, M.; Avila-George, H.; Castro, W. A systematic review of the literature focused on the use of unmanned aerial vehicles during the vegetation detection process. *RISTI - Revista Iberica de Sistemas e Tecnologias de Informacao* **2020**, *2020*, 82–101. https://doi.org/10.17013/risti.36.82-101.
11. Coelho Eugenio, F.; Badin, T.L.; Fernandes, P.; Mallmann, C.L.; Schons, C.; Schuh, M.S.; Soares Pereira, R.; Fantinel, R.A.; Pereira da Silva, S.D. Remotely Piloted Aircraft Systems (RPAS) and machine learning: A review in the context of forest science, 2021. https://doi.org/10.1080/01431161.2021.1975845.
12. Tian, H.; Wang, T.; Liu, Y.; Qiao, X.; Li, Y. Computer vision technology in agricultural automation —A review, 2020. https://doi.org/10.1016/j.inpa.2019.09.006.
13. Azcón-Bieto, J.; Talón, M. Fundamentos de fisiología vegetal, 2003, [arXiv:1011.1669v3].
14. Montero, I.M., Barrera, J.A., Giraldo, B., Lucena, A. Fichas Tecnicas de Especies de uso Forestal y Agroforestal de la Amazonia Colombiana, 2016.
15. Liu, R.; Shang, R.; Liu, Y.; Lu, X. Global evaluation of gap-filling approaches for seasonal NDVI with considering vegetation growth trajectory, protection of key point, noise resistance and curve stability. *Remote Sensing of Environment* **2017**, *189*, 164–179. https://doi.org/10.1016/j.rse.2016.11.023.
16. Cen, H.; Wan, L.; Zhu, J.; Li, Y.; Li, X.; Zhu, Y.; Weng, H.; Wu, W.; Yin, W.; Xu, C.; et al. Dynamic monitoring of biomass of rice under different nitrogen treatments using a lightweight UAV with dual image-frame snapshot cameras. *Plant Methods* **2019**, *15*, 1–17. https://doi.org/10.1186/s13007-019-0418-8.
17. Zhang, X.; Zhang, F.; Qi, Y.; Deng, L.; Wang, X.; Yang, S. New research methods for vegetation information extraction based on visible light remote sensing images from an unmanned aerial vehicle (UAV). *International Journal of Applied Earth Observation and Geoinformation* **2019**, *78*, 215–226. https://doi.org/10.1016/j.jag.2019.01.001.
18. Ma, X.; Feng, J.; Guan, H.; Liu, G. Prediction of chlorophyll content in different light areas of apple tree canopies based on the color characteristics of 3d reconstruction. *Remote Sensing* **2018**, *10*. https://doi.org/10.3390/rs10030429.
19. Wan, L.; Li, Y.; Cen, H.; Zhu, J.; Yin, W.; Wu, W.; Zhu, H.; Sun, D.; Zhou, W.; He, Y. Combining UAV-based vegetation indices and image classification to estimate flower number in oilseed rape. *Remote Sensing* **2018**, *10*. https://doi.org/10.3390/rs10091484.
20. Smith, A.M.; Bourgeois, G.; Teillet, P.M.; Freemantle, J.; Nadeau, C. A comparison of NDVI and MTVI2 for estimating LAI using CHRIS imagery: A case study in wheat. *Canadian Journal of Remote Sensing* **2008**, *34*, 539–548. https://doi.org/10.5589/m08-071.
21. Rouse, J.W.; Riter, S. Erts experiments compiled. *IEEE Transactions on Geoscience Electronics* **1973**, *11*, 3–76. https://doi.org/10.1109/TGE.1973.294284.
22. Jimenez-Sierra, D.A.; Benítez-Restrepo, H.D.; Vargas-Cardona, H.D.; Chanussot, J. Graph-based data fusion applied to: Change detection and biomass estimation in rice crops. *Remote Sensing* **2020**, *12*, 2683. https://doi.org/10.3390/RS12172683.
23. Marin, W.; Mondragon, I.F.; Colorado, J.D. Aerial Identification of Amazonian Palms in High-Density Forest Using Deep Learning. *Forests* **2022**, *13*, 655. https://doi.org/10.3390/f13050655.
24. Devia, C.A.; Rojas, J.P.; Petro, E.; Martinez, C.; Mondragon, I.F.; Patino, D.; Rebolledo, M.C.; Colorado, J. High-Throughput Biomass Estimation in Rice Crops Using UAV Multispectral Imagery. *Journal of Intelligent and Robotic Systems: Theory and Applications* **2019**, *96*, 573–589. https://doi.org/10.1007/s10846-019-01001-5.
25. Xu, W.; Lan, Y.; Li, Y.; Luo, Y.; He, Z. Classification method of cultivated land based on uav visible light remote sensing. *International Journal of Agricultural and Biological Engineering* **2019**, *12*, 103–109. https://doi.org/10.25165/j.ijabe.20191203.4754.

26. García-cervigón, D.; José, J. Estudio de Índices de vegetación a partir de imágenes aéreas tomadas desde UAS / RPAS y aplicaciones de estos a la agricultura de precisión . **2015**. p. 78.
27. Du, M.; Noguchi, N. Monitoring of wheat growth status and mapping of wheat yield's within-field spatial variations using color images acquired from UAV-camera System. *Remote Sensing* **2017**, *9*. https://doi.org/10.3390/rs9030289.
28. Gitelson, A.A.; Viña, A.; Ciganda, V.; Rundquist, D.C.; Arkebauer, T.J. Remote estimation of canopy chlorophyll content in crops. *Geophysical Research Letters* **2005**, *32*, 1–4. https://doi.org/10.1029/2005GL022688.
29. Kanke, Y.; Tubaña, B.; Dalen, M.; Harrell, D. Evaluation of red and red-edge reflectance-based vegetation indices for rice biomass and grain yield prediction models in paddy fields. *Precision Agriculture* **2016**, *17*, 507–530. https://doi.org/10.1007/s11119-016-9433-1.
30. Naito, H.; Ogawa, S.; Valencia, M.O.; Mohri, H.; Urano, Y.; Hosoi, F.; Shimizu, Y.; Chavez, A.L.; Ishitani, M.; Selvaraj, M.G.; et al. Estimating rice yield related traits and quantitative trait loci analysis under different nitrogen treatments using a simple tower-based field phenotyping system with modified single-lens reflex cameras. *ISPRS Journal of Photogrammetry and Remote Sensing* **2017**, *125*, 50–62. https://doi.org/10.1016/j.isprsjprs.2017.01.010.
31. Prabhakara, K.; Dean Hively, W.; McCarty, G.W. Evaluating the relationship between biomass, percent groundcover and remote sensing indices across six winter cover crop fields in Maryland, United States. *International Journal of Applied Earth Observation and Geoinformation* **2015**, *39*, 88–102. https://doi.org/10.1016/j.jag.2015.03.002.
32. Gnyp, M.L.; Miao, Y.; Yuan, F.; Ustin, S.L.; Yu, K.; Yao, Y.; Huang, S.; Bareth, G. Hyperspectral canopy sensing of paddy rice aboveground biomass at different growth stages. *Field Crops Research* **2014**, *155*, 42–55. https://doi.org/10.1016/j.fcr.2013.09.023.
33. Morris, O.J.; Constantinides, A.G. Graph theory for image analysis: An approach based on the shortest spanning tree. *IEE Proceedings F: Communications Radar and Signal Processing* **1986**, *133*, 146–152. https://doi.org/10.1049/ip-f-1.1986.0025.
34. Cousty, J.; Najman, L.; Dias, F.; Serra, J. Morphological filtering on graphs. *Computer Vision and Image Understanding* **2013**, *117*, 370–385. https://doi.org/10.1016/j.cviu.2012.08.016.
35. Farkas, I.J.; Derényi, I.; Barabási, A.L.; Vicsek, T. Spectra of "real-world" graphs: Beyond the semicircle law. *Physical Review E - Statistical Physics, Plasmas, Fluids, and Related Interdisciplinary Topics* **2001**, *64*, 12, [arXiv:cond-mat/0102335]. https://doi.org/10.1103/PhysRevE.64.026704.
36. Fowlkes, C.; Belongie, S.; Chung, F.; Malik, J. Spectral Grouping Using the Nyström Method. *IEEE Transactions on Pattern Analysis and Machine Intelligence* **2004**, *26*, 214–225. https://doi.org/10.1109/TPAMI.2004.1262185.
37. Naranjo-Torres, J.; Mora, M.; Hernández-García, R.; Barrientos, R.J.; Fredes, C.; Valenzuela, A. A review of convolutional neural network applied to fruit image processing, 2020. https://doi.org/10.3390/app10103443.

Willintong Marin is an Electronic Engineer from the University of Cundinamarca with a master's degree in Business Administration, graduated in 2013 from the Externado University of Colombia. He is currently studying for a Doctorate in Engineering at the Pontificia Universidad Javeriana. He is interested in the field of research oriented to precision agriculture to explore alternatives for sustainable use in the Colombian Amazon using Unmanned Aerial Vehicles. With 15 years of professional experience. He has worked in sectors and activities of administration, education and engineering.

Ivan Mondragon studied electric engineering at Universidad Nacional de Colombia, obtaining the degree of Electric Engineer (BSEE) in October 2002. In 2006, he moved to the Computer Vision Group at DISAM -ETSII- Universidad Politécnica de Madrid (Spain) obtaining a Ph.D degree in Automatic and Robotics in November 2011. Since 2013, he is a full time professor and director of the Industrial Automation Technology Center (CTAI), Department of Industrial Engineering at Pontificia Universidad Javeriana. He is currently working on computer vision applied to Unmanned Aerial Vehicles as well as Flexible Manufacturing Systems FMS, Quality Inspection, virtual reality (CAVE system) and Industry 4.0.

 doi:10.20944/preprints202304.0496.v1

Julian D. Colorado is an Associate Professor in the Department of Electronics Engineering at Pontificia Universidad Javeriana in Bogota, Colombia. He completed his Ph.D and M.Sc. in Robotics at Universidad Politecnica de Madrid in Spain, where he studied the development of novel flight controllers for a diverse category of Unmanned Aerial Vehicles, including quad-rotors and highly-articulated morphing wing drones inspired by the biomechanics of bats. He was a visiting research fellow at Brown University, USA (2010–2011), where he studied how to integrate smart-actuators based on Shape Memory Alloys to control wing modulation in a bat-like UAV. Julian Colorado research interests include Field Robotics, Aerial Robotics, Bio-inspired robotics and Guidance Navigation Control –GNC.